

Article

New Low-Sn Zr Cladding Alloys with Excellent Autoclave Corrosion Resistance and High Strength

Ruiqian Zhang ¹, Beibei Jiang ², Chang Pang ², Xun Dai ¹, Yongduo Sun ¹, Wei Liao ¹, Qing Wang ^{2,*} and Chuang Dong ²

¹ Science and Technology on Reactor Fuel and Materials Laboratory, Nuclear Power Institute of China, Chengdu 610213, China; zhang_ruiqian@126.com (R.Z.); daixun82@aliyun.com (X.D.); redclupeoid@163.com (Y.S.); liaowei@cnc.com.cn (W.L.)

² Key Laboratory of Materials Modification by Laser, Ion and Electron Beams (Ministry of Education), School of Materials Science and Engineering, Dalian University of Technology, Dalian 116024, China; babywhrs@126.com (B.J.); aianor@163.com (C.P.); dong@dlut.edu.cn (C.D.)

* Correspondence: wangq@dlut.edu.cn; Tel.: +86-411-8470-8615

Academic Editor: Laichang Zhang

Received: 21 March 2017; Accepted: 17 April 2017; Published: 19 April 2017

Abstract: It is expected that low-Sn Zr alloys are a good candidate to improve the corrosion resistance of Zr cladding alloys in nuclear reactors, presenting excellent corrosion resistance and high strength. The present work developed a new alloy series of Zr-0.25Sn-0.36Fe-0.11Cr-*x*Nb (*x* = 0.4~1.2 wt %) to investigate the effect of Nb on autoclave corrosion resistance. Alloy ingots were prepared by non-consumable arc-melting, solid-solutioned, and then rolled into thin plates with a thickness of 0.7 mm. It was found that the designed low-Sn Zr alloys exhibit excellent corrosion resistances in three out of pile autoclave environments (distilled water at 633 K/18.6 MPa, 70 ppm LiOH solution at 633 K/18.6 MPa, and superheated water steam at 673 K/10.3 MPa), as demonstrated by the fact of the Zr-0.25Sn-0.36Fe-0.11Cr-0.6Nb alloy shows a corrosion weight gain $\Delta G = 46.3 \text{ mg/dm}^2$ and a tensile strength of $\sigma_{\text{UTS}} = 461 \text{ MPa}$ following 100 days of exposure in water steam. The strength of the low-Sn Zr alloy with a higher Nb content (*x* = 1.2 wt %) is enhanced up to 499 MPa, comparable to that of the reference high-Sn N36 alloy (Zr-1.0Sn-1.0Nb-0.25Fe, wt %). Although the strength improvement is at a slight expense of corrosion resistance with the increase of Nb, the corrosion resistance of the high-Nb alloy with *x* = 1.2 ($\Delta G = 90.4 \text{ mg/dm}^2$ for 100-day exposure in the water steam) is still better than that of N36 ($\Delta G = 103.4 \text{ mg/dm}^2$).

Keywords: low-Sn Zr cladding materials; Zr-Sn-Fe-Cr-Nb alloys; mechanical property; corrosion resistance

1. Introduction

As fuel cladding and structural materials for commercial nuclear reactors, Zr alloys exhibit excellent radiation-resistance and good corrosion-resistance and mechanical properties in a neutron reactor environment lower than 623 K [1–3]. Such alloys with high performance were the main focus in Zr-Sn and Zr-Nb series [4–10], e.g., Zr-1.0Sn-1.0Nb-0.1Fe (ZIRLO alloy, the number before each element represents the weight percent, wt %), Zr-1.0Nb-O (M5), Zr-1.2Sn-1.0Nb-0.35Fe (E635), and Zr-1.0Sn-1.0Nb-0.25Fe (N36). They were generally minor-alloyed with multiple solute elements to achieve the optimum comprehensive properties. In order to further improve the waterside corrosion resistance, several Zr alloys with a much lower content of Sn were expected to be developed, such as Zr-0.4Sn-0.2Fe-0.1Cr-1.5Nb (HANA-4) [1] and Zr-0.66Sn-1.0Nb-0.1Fe, modified from ZIRLO alloy [11].

It is emphasized that the mechanical strength and the corrosion resistance of Zr alloys are closely related to the types and amounts of alloying elements [12–17]. It is difficult to achieve high

strength and excellent corrosion resistance simultaneously through adding one or two elements since these two requirements are incompatible. For instance, the element Sn promotes the solid-solution strengthening, while its excessive content could deteriorate the corrosion resistance [3,11]. Fe, Cr, and Nb elements are always precipitated from the α -Zr matrix to form the second phases, such as $Zr(Fe,Cr)_2$ and β -Nb, which can enhance the mechanical properties of alloys at the expense of the corrosion resistance [4–10,18–23]. Actually, different Fe/Cr ratios in the $Zr(Fe,Cr)_2$ phase can also induce different corrosion resistance in the Fe/Cr-containing Zr alloys [5]. Thus, for low-Sn Zr alloys, the contents of other alloying elements should be adjusted to ensure the mechanical properties, as demonstrated by the fact that increasing the Fe content indeed enhances the strengths of Zr-1.0Nb- x Fe alloy series [24].

By far, the mechanical and autoclave corrosion-resistant properties of Zr alloys with a much lower Sn content have been seldom reported. Therefore, the present work will aim at developing a new low-Sn Zr alloy series of Zr-0.25Sn-0.36Fe-0.11Cr- x Nb, in which the Nb content is varied and the Fe and Cr contents are fixed and referred from the present in-pile N18 alloy (Zr-1.0Sn-0.35Fe-0.11Cr-0.35Nb) due to the suitable Fe/Cr ratio [5]. The microstructural characterization, tensile mechanical property, and autoclave corrosion resistances in three corrosive mediums of the designed alloy series will be performed comprehensively to evaluate the effect of Nb element on the properties. The high-Sn N36 alloy (Zr-1.0Sn-0.25Fe-1.0Nb) with a higher strength and good corrosion resistance is taken here as the reference alloy. It would be verified that this series of new low-Sn Zr alloys will possess prominent autoclave corrosion resistances and high strengths.

2. Experimental Section

The alloy ingots of the designed low-Sn alloy series of Zr-0.25Sn-0.36Fe-0.11Cr- x Nb ($x = 0.4, 0.6, 0.8, \text{ and } 1.2$, called Z- x Nb hereafter), as well as the reference N36, were prepared by non-consumably arc-melting the mixtures of Zr, Fe, Cr, Sn, and Nb with a purity of 99.99% in the Ti-gettered high-purity argon atmosphere. These ingots with a weight of about 50 g were flipped and remelted at least five times to ensure chemical homogeneity. They were then solid-solutioned at 1323 K for 0.5 h under a vacuum condition plus water-quenching. In the following, all the ingots were hot rolled into plates a thickness of 2 mm at 873 K eight times, in which the surface of the plates was cut mechanically for the deletion of the oxidation layer. Alloy plates were resealed into a vacuum quartz cube for further heat-treatment at 853 K for 1 h and then cold-rolled into thin plates with a thickness of 0.7 mm three times. Finally, these thin plates were heat-treated at 833 K for 2 h under a vacuum condition. All the heat treatments and rolling processing were taken from those for the reference N36 alloy.

Structural identification was performed by the Bruker D8 Focus X-ray diffraction (XRD, Ettlingen, Germany) using the Cu K_{α} radiation ($\lambda = 0.15406$ nm), in which the Jade software was used to fit the diffraction peaks [25]. The microstructure morphology and phase verification were carried on with the Philips Tecnai G² transmission electron microscopy (TEM, Amsterdam, the Netherlands) with the selected-area electron diffraction (SAED) analysis, where the TEM samples were prepared by twin-jet electro-polishing in a solution of 12% HClO₄ + 88% C₂H₅OH (volume fraction) at 243 K. Tensile tests were performed at room temperature with a strain rate of $3.5 \times 10^{-4} \text{ s}^{-1}$ by using a MTS-810 tensile testing machine (MTS, Cary, NC, USA). The tensile specimens were machined along the rolling direction with a gauge size of 24×4 mm (length \times width), in which four tensile specimens were prepared for each composition alloy. The autoclave corrosion tests were conducted under three out-of-pile conditions, i.e., distilled water at 633 K with a pressure of 18.6 MPa, 70 ppm LiOH aqueous solution at 633 K with a pressure of 18.6 MPa, and superheated water steam at 673 K with a pressure of 10.3 MPa, respectively. The specimens for corrosion testing are rectangular with a size of 20×30 mm and three specimens for each alloy under each condition were prepared, in which the sample surfaces were ground to 1200-grit SiC paper. The corrosion resistance of the specimens was evaluated by measuring the weight gain per unit surface area in relation to the exposure time.

3. Results and Discussion

3.1. Microstructure Characterization

The XRD results (Figure 1) show that all the designed Zr-0.25Sn-0.36Fe-0.11Cr- x Nb (Z- x Nb) alloys, as well as the reference N36 alloy, exhibit a single hexagonal α -Zr structure. The lattice constants were calculated by single-peak fitting the (002), (101), and (102) peaks respectively with the Pearson VII function in Jade, and the average values with errors were listed in Table 1. For further identification of the second precipitated phases, the TEM observations were executed, as shown in Figure 2. It could be found that these precipitated particles are distributed uniformly on the α -Zr matrix, and the amount of precipitates increases with the Nb content from $x = 0.4$ to $x = 1.2$ (Figure 2a–d). The particle sizes in all these alloys are almost constant, being about 50–100 nm. In the Z-0.4Nb alloy (Figure 2a), the precipitates are scarce, indicating that the alloying elements are almost soluble in the α -Zr matrix. While in the other Zr- x Nb alloys with $x = 0.8$ – 1.2 , the amounts of the precipitates are relatively higher, more than that in the N36 alloy (Zr-1.0Sn-1.0Nb-0.25Fe) with a high Sn content (Figure 2b–e).

Table 1. Compositions of the designed low-Sn Z- x Nb alloy series and the lattice constants of the hexagonal HCP α -Zr matrix, as well as their mechanical tensile properties (σ_{YS} : yield strength, σ_{UTS} : ultimate tensile strength, δ : elongation to fracture).

Compositions		Lattice Constants		σ_{YS} (MPa)	σ_{UTS} (MPa)	δ (%)
(wt %)	(at %)	a (nm)	c (nm)			
Zr-0.25Sn-0.36Fe-0.11Cr-0.40Nb (Z-0.4Nb)	Zr _{98.63} Sn _{0.20} Nb _{0.39} Fe _{0.59} Cr _{0.20}	0.3228 ± 0.0001	0.5137 ± 0.0001	365	458	26.5
Zr-0.25Sn-0.36Fe-0.11Cr-0.60Nb (Z-0.6Nb)	Zr _{98.44} Sn _{0.20} Nb _{0.59} Fe _{0.59} Cr _{0.20}	0.3229 ± 0.0003	0.5137 ± 0.0001	380	461	18.6
Zr-0.25Sn-0.36Fe-0.11Cr-0.80Nb (Z-0.8Nb)	Zr _{98.24} Sn _{0.20} Nb _{0.78} Fe _{0.59} Cr _{0.20}	0.3229 ± 0.0002	0.5146 ± 0.0001	373	456	20.2
Zr-0.25Sn-0.36Fe-0.11Cr-1.20Nb (Z-1.2Nb)	Zr _{97.85} Sn _{0.20} Nb _{1.17} Fe _{0.59} Cr _{0.20}	0.3229 ± 0.0003	0.5146 ± 0.0001	425	499	18.4
Zr-1.0Sn-0.25Fe-1.0Nb (N36 (Ref.))	Zr _{97.85} Sn _{0.78} Nb _{0.98} Fe _{0.39}	0.3226 ± 0.0003	0.5137 ± 0.0001	422	489	22.3

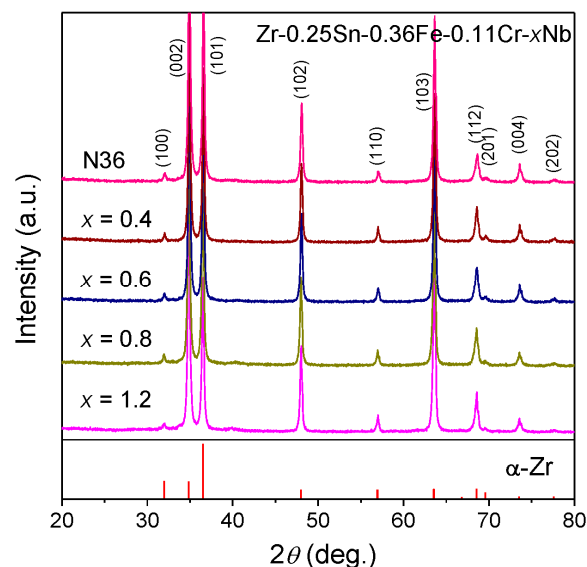


Figure 1. XRD patterns of the designed low-Sn Zr-0.25Sn-0.36Fe-0.11Cr- x Nb (Z- x Nb) alloys and the reference N36.

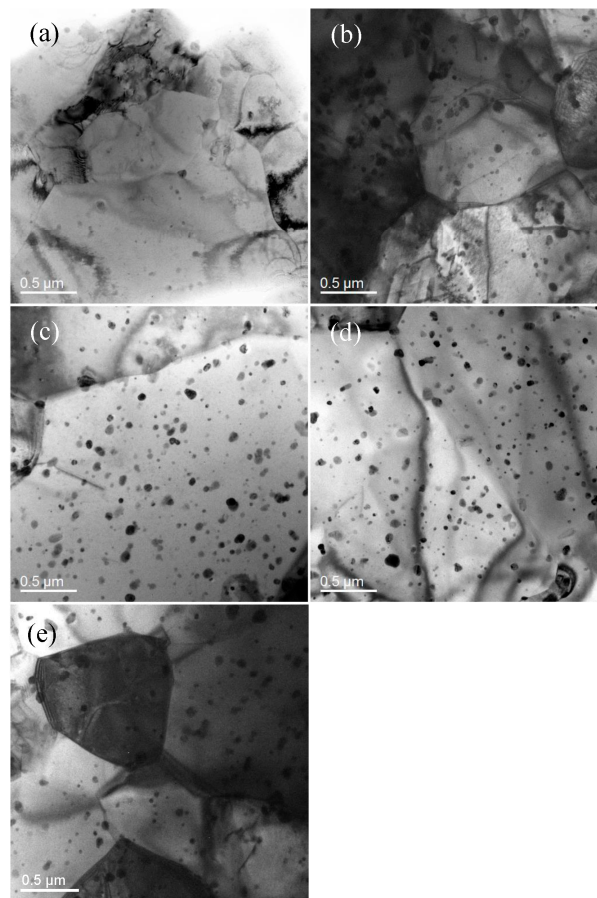


Figure 2. TEM bright field images of the designed Zr-0.25Sn-0.36Fe-0.11Cr- x Nb alloys, (a) $x = 0.4$; (b) $x = 0.6$; (c) $x = 0.8$; (d) $x = 1.2$; and (e) N36.

The selected-area electron diffraction (SAED) analysis of TEM indicates that on the α -Zr matrix, the second precipitates are identified as a Laves phase $\text{Zr}(\text{Fe,Cr,Nb})_2$ with a hexagonal structure. Specifically, Figure 3a gives the TEM results of the Z-0.4Nb alloy with a minor amount of second particles, showing the matrix with a hexagonal structure in $[111]_\alpha$ direction (Figure 3b). The spherical particles in the Z-1.2Nb alloy also exhibit a hexagonal structure, identified as the Laves $\text{Zr}(\text{Fe,Cr,Nb})_2$ phase by the SAED pattern with the $[341]$ direction (Figure 3c,d). The lattice constants of the precipitates in the Z-1.2Nb are $a = 0.502$ nm and $c = 0.818$ nm, respectively, close to those reported values of Laves phases of $\text{Zr}(\text{Fe,Cr,Nb})_2$ ($a = 0.54$ nm, $c = 0.87$ nm) in the Zr-1.6Sn-0.6Nb-0.2Fe-0.1Cr alloy [18].

According to the lattice constants of the α -Zr matrix in this Z- x Nb alloy series listed in Table 1, it could be found that the lattice constants (a and c) increase gradually with the Nb content from $x = 0.4$ to $x = 1.2$. It results from the precipitation of the solutes in the form of intermetallic compound since the atomic radii of all the solutes are smaller than that of Zr, being $R_{\text{Sn}} = 0.140$ nm, $R_{\text{Nb}} = 0.147$ nm, $R_{\text{Fe}} = 0.127$ nm, $R_{\text{Cr}} = 0.128$ nm, and $R_{\text{Zr}} = 0.160$ nm [26], respectively. Among them, the atomic radii of Nb, Fe, Cr, and Zr are Goldschmidt radii, while that of Sn is a covalent radius due to the strong interaction between Sn and Zr (larger negative enthalpy of mixing $\Delta H = -43$ kJ/mol [26]). It was also confirmed by the TEM results that the amount of the second particles in this alloy series increases with Nb (Figure 2a–d). However, the largest lattice constants ($a = 0.3229$ nm and $c = 0.5146$ nm) of the Z-0.8Nb and Z-1.2Nb alloys are slightly lower than that of pure Zr ($a = 0.3232$ nm and $c = 0.5148$ nm [27]), implying that a certain amount of solute elements (Sn and Nb) is still solid-solutioned into the matrix. In comparison, the lattice constants ($a = 0.3226$ nm and $c = 0.5137$ nm) of the reference N36 alloy with a high Sn is the smallest, smaller than that of the Z-0.4Nb alloy,

which because a much higher content of Sn could be soluble in the matrix due to large solubility (about 1.2 wt %) of Sn in α -Zr [18–20].

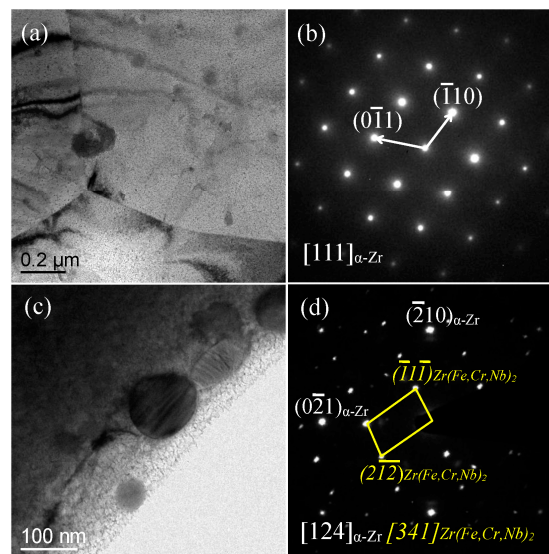


Figure 3. TEM bright field images and SAED patterns of typical serial alloys. (a,b) Zr-0.25Sn-0.36Fe-0.11Cr-0.4Nb; and (c,d) Zr-0.25Sn-0.36Fe-0.11Cr-1.2Nb.

3.2. Mechanical Tensile Properties

The engineering tensile stress-strain curves of the designed Zr-xNb alloys and the reference N36 alloy are shown in Figure 4, from which the mechanical property parameters, including the yield strength σ_{YS} , the ultimate tensile strength σ_{UTS} , and the elongation to fracture δ , could be obtained. All these values are listed in Table 1. Figure 5 gives the variation tendencies of σ_{YS} , σ_{UTS} , and δ of these alloys with the Nb content, in which the strengths of Zr alloys keep at a relatively lower level (σ_{UTS} ~460 MPa) when the Nb content is not more than 0.80 wt %. The Z-0.4Nb alloy with the lowest Nb content in this series has the best tensile ductility with $\delta = 26.5\%$. When Nb increases to $x = 1.2$ wt %, the alloy strength is enhanced obviously by precipitation strengthening, as demonstrated by the fact that the Z-1.2Nb alloy shows the highest strength with $\sigma_{YS} = 425$ MPa and $\sigma_{UTS} = 499$ MPa, comparable to that of the reference N36 alloy ($\sigma_{YS} = 422$ MPa and $\sigma_{UTS} = 489$ MPa) measured under the same condition. It indicates that the increase of Nb in low-Sn Zr alloys can also achieve a relatively higher strength. In addition, all of these alloys possess good ductility with the $\delta = 18\sim 27\%$.

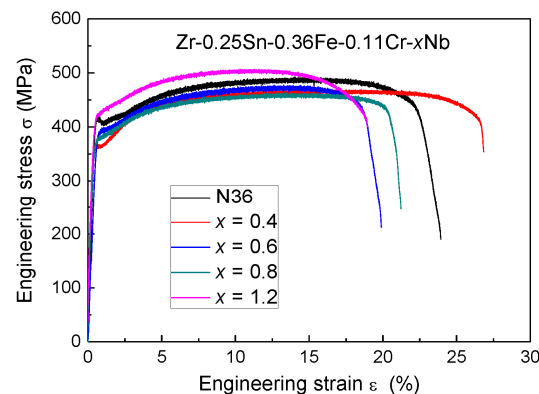


Figure 4. Engineering tensile stress-strain curves of the designed serial Zr-0.25Sn-0.36Fe-0.11Cr-xNb alloys.

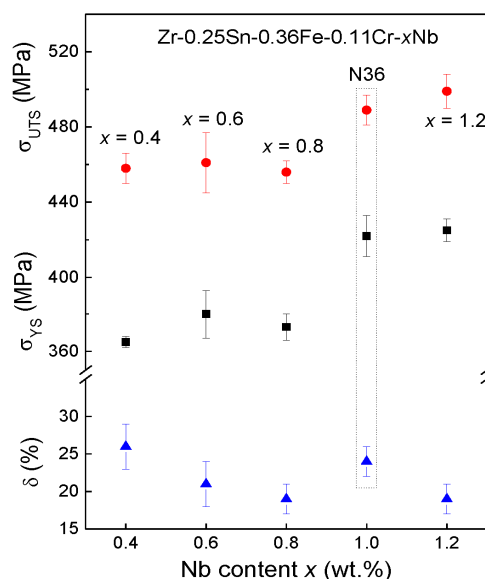


Figure 5. Variations of mechanical properties vs. the Nb content in the designed low-Sn Zr-0.25Sn-0.36Fe-0.11Cr-xNb alloy series.

3.3. Autoclave Corrosion Resistances

In order to investigate the general autoclave corrosion behaviors of the designed low-Sn Zr-xNb alloys, the corrosion weight gains of these alloys and N36 were measured in the distilled water at 633 K/18.6 MPa, as shown in Figure 6a. It can be seen that the corrosion behaviors of this low-Sn Zr alloy series change with increasing Nb content. For the reference N36 alloy with a high content of Sn, the corrosion weight gain ΔG increases slowly before the 150-day exposure and is then enhanced sharply, as evidenced by the $\Delta G = 86.8 \text{ mg/dm}^2$ after exposure for 324 days. The corrosion gains of all the designed low-Sn Zr-xNb alloys are lower than that of N36. Specially, the Z-xNb alloys with a low Nb content ($x \leq 0.6$) exhibit the excellent corrosion resistance, in which the ΔG s are about 44 mg/dm^2 after the 324-day exposure, only half of that of N36. With increasing the Nb content (0.8–1.2 wt %), the corrosion weight gains of alloys are increased, being 63 mg/dm^2 (Z-0.8Nb) and 80 mg/dm^2 (Z-1.2Nb), respectively.

The corrosion behaviors of this low-Sn Zr alloy series in the 70 ppm LiOH aqueous solution at 633 K/18.6 MPa (the simulated in-pile hydrochemical condition) follow a similar variation tendency with the Nb content to that in the distilled water, as shown in Figure 6b. The reference alloy N36 undergoes a corrosion transition at about 125 days of exposure, and then the corrosion gain increases significantly, with a ΔG of 93.1 mg/dm^2 after tested for 283 days. The low-Sn and low-Nb alloys (Z-0.4Nb and Z-0.6Nb) still possess the excellent corrosion resistance with a ΔG of about 63.5 mg/dm^2 for 283-day exposure, which is about 70% of the N36. The corrosion resistances of the high-Nb alloys (Z-0.8Nb and Z-1.2Nb) are inferior to those of the low-Nb alloys, but still better than that of N36, in which the corrosion weight gains are within the range of $72.4\text{--}86.2 \text{ mg/dm}^2$ for the 283-day exposure.

In order to further study the uniform corrosion behavior of these designed alloys, the 100-day corrosion tests were carried out in superheated water steam at 673 K/10.3 MPa, and the corrosion weight gain curves are shown in Figure 6c. The corrosion rate of the reference N36 was accelerated after the 40-day exposure, and the ΔG reached 103.4 mg/dm^2 for the 100-day exposure. In comparison, the corrosion resistances of the low-Sn Zr alloys are obviously better than that of the N36. Similarly, the low-Sn and low-Nb alloys (Z-0.4Nb and Z-0.6Nb) have excellent corrosion resistance with ΔG s of only about 47.0 mg/dm^2 after the 100-day exposure, less than half of that of the N36. Increasing Nb would reduce the corrosion resistances, as demonstrated by the fact that the ΔG of the Z-1.2Nb alloy increases up to 90.4 mg/dm^2 .

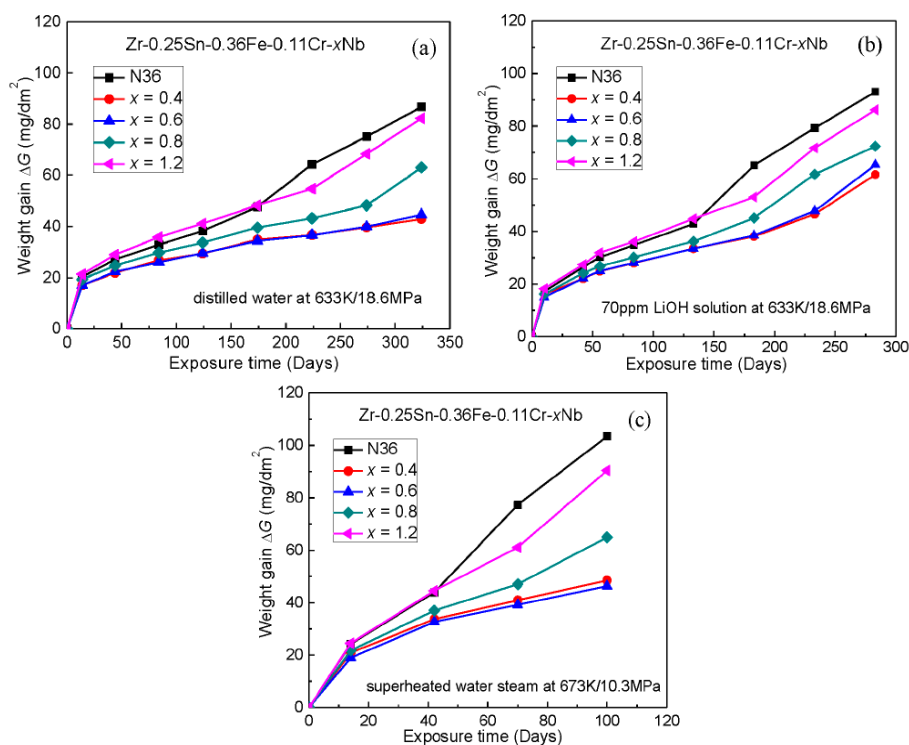


Figure 6. Corrosion behavior of the designed low-Sn Zr-0.25Sn-0.36Fe-0.11Cr-xNb alloys in different out of pile autoclave environments. (a) distilled water at 633 K/18.6 MPa; (b) 70 ppm LiOH solution at 633 K/18.6 MPa; and (c) superheated water steam at 673 K/10.3 MPa.

Since the variation tendencies of corrosion weight gains ΔG of the designed low-Sn Zr-xNb alloys in the present three corrosion environments with the Nb content are similar, the variation of the ΔG vs. the Nb content in the superheated water steam at 673 K/10.3 MPa for 100-day exposure is specially shown in Figure 7a. It could be found that the ΔG values of these designed alloys increase with the Nb, indicating that the corrosion resistance of these low-Sn alloys would be reduced with the amount of precipitates increasing. Among them, the corrosion gains ΔG of the Z-(0.4~0.6)Nb alloys are the minimum, about 47.0 mg/dm² for 100-day exposure. Although the ΔG of the Z-1.2Nb alloy with a higher Nb is the maximum ($\Delta G = 103.4$ mg/dm²) in this designed series, it exhibits a better corrosion resistance than the reference N36 alloy ($\Delta G = 103.4$ mg/dm²).

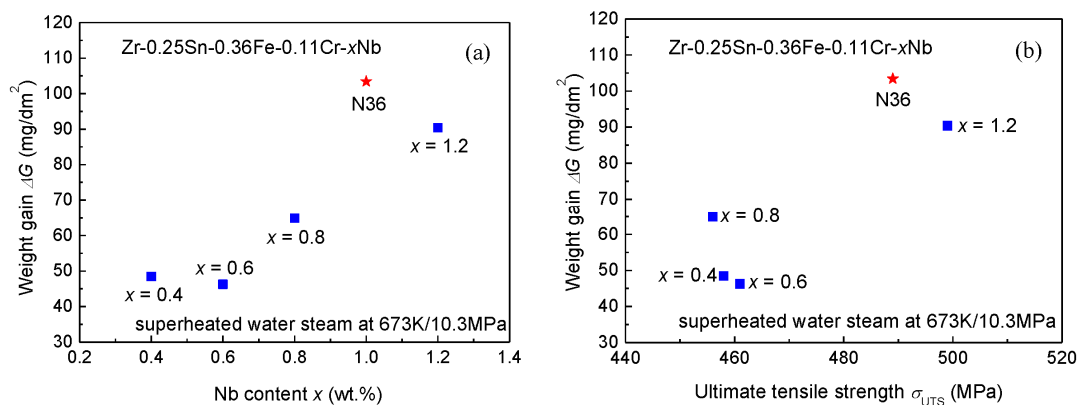


Figure 7. Variation of the corrosion weight gain ΔG in the superheated water steam at 673 K/10.3 MPa for 100-day exposure vs. the Nb content (a) and ultimate tensile strength σ_{UTS} ; (b) of the designed low-Sn Zr-0.25Sn-0.36Fe-0.11Cr-xNb alloys.

Moreover, Table 1 also gives the atomic percent expression of the designed alloys and the reference N36. It is found that the Zr-1.2Nb alloy contains the same content of solute elements (2.15 at %) as the N36, as a result that the tensile strengths of these two alloys are comparable strengthened by both solid solution and precipitation [28]. While the better corrosion resistance of the Zr-1.2Nb alloy in above three autoclave corrosion environments is due to a much smaller amount of Sn (0.20 at %) soluble in the α -Zr matrix, in comparison to that of the N36 alloy containing a high soluble Sn content of 0.78 at % [18–20].

According to the strength and corrosion resistance of the designed low-Sn Zr-xNb alloys, as shown in Figure 7b—being the relationship of the σ_{UTS} with the ΔG (in the superheated water steam at 673 K/10.3 MPa for 100-day exposure)—these alloys could be classified into two groups. One group (Nb \leq 0.8 wt %) exhibits the excellent corrosion resistance with a strength level of $\sigma_{\text{UTS}} = 460$ MPa, and the other shows a higher strength ($\sigma_{\text{UTS}} = 499$ MPa) and better corrosion resistance than the reference high-Sn N36 alloy (Zr-1.0Sn-1.0Nb-0.25Fe, $\sigma_{\text{UTS}} = 489$ MPa). Furthermore, the corrosion resistances under various environments of these low-Sn alloys are all better than that of the N36.

4. Conclusions

A new low-Sn Zr cladding alloy series of Zr-0.25Sn-0.36Fe-0.11Cr-xNb with high strength and excellent corrosion resistance were developed by changing Nb content ($x = 0.4, 0.6, 0.8, 1.2$). The designed low-Sn alloys exhibit excellent corrosion resistances in three out-of-pile autoclave environments (distilled water at 633 K/18.6 MPa, 70 ppm LiOH solution at 633 K/18.6 MPa, and superheated water steam at 673 K/10.3 MPa), as exemplified by the Zr-0.25Sn-0.36Fe-0.11Cr-0.6Nb alloy (wt %) with the corrosion weight gain $\Delta G = 46.3$ mg/dm² for 100-day exposure in the superheated water steam environment and with a tensile strength of $\sigma_{\text{UTS}} = 460$ MPa. A large amount of precipitates on the α -Zr matrix with an increase of Nb can enhance the strength of these low-Sn alloys up to $\sigma_{\text{UTS}} = 499$ MPa, comparable to that of the reference high-Sn N36 alloy (Zr-1.0Sn-1.0Nb-0.25Fe wt %, $\sigma_{\text{UTS}} = 489$ MPa). More importantly, all the corrosion resistance of these high-strength and low-Sn alloys (e.g., Zr-0.25Sn-0.36Fe-0.06Cr-1.2Nb with $\Delta G = 90.4$ mg/dm² for 100-day exposure in the water steam at 674 K/10.3 MPa) is still better than that of N36 ($\Delta G = 103.4$ mg/dm² under the same condition).

Acknowledgments: This work was supported by the International Thermonuclear Experimental Reactor (ITER) Program of China [No. 2015GB121004], the International Science & Technology Cooperation Program of China [No. 2015DFR60370], the Natural Science Foundation of Liaoning Province of China [No. 2015020202], and the Fundamental Research Funds for the Central Universities [No. DUT16ZD212].

Author Contributions: Ruiqian Zhang and Qing Wang conceived and designed the experiments and wrote the paper; Chang Pang and Beibei Jiang performed the experiments and analyzed the data; Xun Dai, Yongduo Sun, and Wei Liao provided assistance in the experiments and contributed reagents/materials; Chuang Dong modified the paper.

Conflicts of Interest: The authors declare no conflicts of interest.

References

1. Park, J.-Y.; Yoo, S.J.; Choi, B.-K.; Jeong, Y.H. Corrosion and oxide characteristics of Zr-1.5Nb-0.4Sn-0.2Fe-0.1Cr alloys in 360 °C pure water and LiOH solution. *J. Nucl. Mater.* **2008**, *373*, 343–350. [[CrossRef](#)]
2. Yao, M.Y.; Zhou, B.X.; Li, Q.; Liu, W.Q.; Geng, X.; Lu, Y.P. A superior corrosion behavior of Zircaloy-4 in lithiated water at 360 °C/18.6 MPa by β -quenching. *J. Nucl. Mater.* **2008**, *374*, 197–203. [[CrossRef](#)]
3. Thorvaldsson, T.; Andersson, T.; Wilson, A.; Wardle, A. Correlation between 400 °C steam corrosion behavior, heat treatment, and microstructure of Zircaloy-4 tubing. In *Zirconium in the Nuclear Industry: Eighth International Symposium*; Van Swam, L.F.P., Eucken, C.M., Eds.; ASTM International: Baltimore, MD, USA, 1989; pp. 128–140.
4. Kim, H.G.; Jeong, Y.H.; Kim, T.H. Effect of isothermal annealing on the corrosion behavior of Zr-xNb alloys. *J. Nucl. Mater.* **2004**, *326*, 125–131. [[CrossRef](#)]
5. Zhao, W.; Liu, Y.; Jiang, H.; Peng, Q. Effect of heat treatment and Nb and H contents on the phase transformation of N18 and N36 zirconium alloys. *J. Alloys Compd.* **2008**, *462*, 103–108. [[CrossRef](#)]

6. Sabol, G.P. ZIRLO™—An Alloy Development Success. In *Zirconium in the Nuclear Industry: 14th International Symposium*; Ruding, P., Kammenzind, B., Eds.; ASTM International: Bridgeport, CT, USA, 2005; Volume 2, pp. 3–24.
7. Bossis, P.; Pecheur, D.; Hanifi, K.; Thomazet, J.; Blat, M. Comparison of the high burn-up corrosion on M5 and low tin Zircaloy-4. In *Zirconium in the Nuclear Industry: 14th International Symposium*; Ruding, P., Kammenzind, B., Eds.; ASTM International: Bridgeport, CT, USA, 2005; Volume 3, pp. 494–525.
8. Shishov, V.; Peregud, M.; Nikulina, A.; Kon'kov, V.; Novikov, V.; Markelov, V.; Khokhunova, T.; Kobylansky, G.; Novoselov, A.; Ostrovsky, Z. Structure-phase state, corrosion and irradiation properties of Zr-Nb-Fe-Sn system alloys. In *Zirconium in the Nuclear Industry: 15th International Symposium*; Kammenzind, B., Limbäck, M., Eds.; ASTM International: Baltimore, MD, USA, 2009; Volume 5, pp. 724–743.
9. Yamate, K.; Oe, A.; Hayashi, M.; Okamoto, T.; Anada, H.; Hagi, S. Burnup extension of Japanese PWR fuels. In Proceedings of the 1997 International Topical Meeting on LWR Fuel Performance Conference, Portland, OR, USA, 2–6 March 1997; pp. 318–325.
10. Zhou, B.X.; Yao, M.Y.; Li, Z.K.; Wang, X.M.; Zhou, J.; Long, C.S.; Liu, Q.; Luan, B.F. Optimization of N18 zirconium alloy for fuel cladding of water reactors. *J. Mater. Sci. Technol.* **2012**, *28*, 606–613. [[CrossRef](#)]
11. Wei, J.; Frankel, P.; Polatidis, E.; Blat, M.; Ambard, A.; Comstock, R.; Hallstadius, L.; Hudson, D.; Smith, G.; Grovenor, C. The effect of Sn on autoclave corrosion performance and corrosion mechanisms in Zr-Sn-Nb alloys. *Acta Mater.* **2013**, *61*, 4200–4214. [[CrossRef](#)]
12. Chun, Y.B.; Hwang, S.K.; Kim, M.H.; Kwun, S.I.; Kim, Y.S. Effect of Mo on recrystallization characteristics of Zr-Nb-(Sn)-Mo experimental alloys. *J. Nucl. Mater.* **1999**, *265*, 28–37. [[CrossRef](#)]
13. Shishov, V.N.; Peregud, M.M.; Nikulina, A.V.; Pimenov, Y.V.; Kobylansky, G.P.; Novoselov, A.E.; Ostrovsky, Z.E.; Obukhov, A.V. Influence of Structure—Phase State of Nb Containing Zr Alloys on Irradiation-Induced Growth. In *Zirconium in the Nuclear Industry: 14th International Symposium*; Ruding, P., Kammenzind, B., Eds.; ASTM International: Bridgeport, CT, USA, 2005; Volume 2, pp. 1–18.
14. Kim, Y.-S.; Kim, S.-K.; Bang, J.-G.; Jung, Y.-H. Effects of Sn and Nb on massive hydriding kinetics of Zr-XSn-YNb alloy. *J. Nucl. Mater.* **2000**, *279*, 335–343. [[CrossRef](#)]
15. Wadekar, S.; Raman, V.; Banerjee, S.; Asundi, M. Structure-property correlation of Zr-base alloys. *J. Nucl. Mater.* **1988**, *151*, 162–171. [[CrossRef](#)]
16. Pêcheur, D. Oxidation of β -Nb and Zr(Fe,V)₂ precipitates in oxide films formed on advanced Zr-based alloys. *J. Nucl. Mater.* **2000**, *278*, 195–201. [[CrossRef](#)]
17. Steinbrück, M.; Böttcher, M. Air oxidation of Zircaloy-4, M5[®] and ZIRLO[™] cladding alloys at high temperatures. *J. Nucl. Mater.* **2011**, *414*, 276–285. [[CrossRef](#)]
18. Shen, H.; Peng, S.; Xiang, X.; Naab, F.; Sun, K.; Zu, X. Proton irradiation effects on the precipitate in a Zr-1.6Sn-0.6Nb-0.2Fe-0.1Cr alloy. *J. Nucl. Mater.* **2014**, *452*, 335–342. [[CrossRef](#)]
19. Liu, W.; Li, Q.; Zhou, B.; Yan, Q.; Yao, M. Effect of heat treatment on the microstructure and corrosion resistance of a Zr-Sn-Nb-Fe-Cr alloy. *J. Nucl. Mater.* **2005**, *341*, 97–102. [[CrossRef](#)]
20. Hong, H.S.; Moon, J.S.; Kim, S.J.; Lee, K.S. Investigation on the oxidation characteristics of copper-added modified Zircaloy-4 alloys in pressurized water at 360 °C. *J. Nucl. Mater.* **2001**, *297*, 113–119. [[CrossRef](#)]
21. Lelievre, G.; Tessier, C.; Iltis, X.; Berthier, B.; Lefebvre, F. Impact of intermetallic precipitates on hydrogen distribution in the oxide layers formed on zirconium alloys in a steam atmosphere: A ²D (³He, p) α nuclear analysis study in microbeam mode. *J. Alloys Compd.* **1998**, *268*, 308–317. [[CrossRef](#)]
22. Toffolon-Masclat, C.; Brachet, J.-C.; Jago, G. Studies of second phase particles in different zirconium alloys using extractive carbon replica and an electrolytic anodic dissolution procedure. *J. Nucl. Mater.* **2002**, *305*, 224–231. [[CrossRef](#)]
23. Jeong, Y.H.; Kim, H.G.; Kim, T.H. Effect of β phase, precipitate and Nb-concentration in matrix on corrosion and oxide characteristics of Zr-xNb alloys. *J. Nucl. Mater.* **2003**, *317*, 1–12. [[CrossRef](#)]
24. Shishov, V.N. The evolution of microstructure and deformation stability in Zr-Nb-(Sn, Fe) alloys under neutron irradiation. In *Zirconium in the Nuclear Industry: 16th International Symposium*; Limbäck, M., Barbéris, P., Eds.; ASTM International: Baltimore, MD, USA, 2012; Volume 7, pp. 200–213.
25. Waseda, Y.; Matsubara, E.; Shinoda, K. *X-ray Diffraction Crystallography*; Springer: Heidelberg, Germany, 2011; pp. 107–127.

26. Takeuchi, A.; Inoue, A. Classification of bulk metallic glasses by atomic size difference, heat of mixing and period of constituent elements and its application to characterization of the main alloying element. *Mater. Trans.* **2005**, *46*, 2817–2829. [[CrossRef](#)]
27. Russell, R.B. Coefficients of thermal expansion for zirconium. *J. Metals* **1954**, *6*, 1045–1052.
28. Curtis, R.E.; Dressier, G. Effect of thermomechanical processing and heat treatment on the properties of Zr-3Nb-1Sn strip and tubing. In *Zirconium in the Nuclear Applications*; Schemel, J.H., Rosenbaum, H.S., Eds.; ASTM International: Harrisburg, PA, USA, 1974; Volume 551, pp. 104–128.



© 2017 by the authors. Licensee MDPI, Basel, Switzerland. This article is an open access article distributed under the terms and conditions of the Creative Commons Attribution (CC BY) license (<http://creativecommons.org/licenses/by/4.0/>).